Extended Abstract for 32nd AIAA Applied Aerodynamics Conference, 16-20 June 2014

Aeroelastic Modeling of a Nozzle Startup Transient

Ten-See Wang*
NASA Marshall Space Flight Center, Huntsville, Alabama, 35812

Xiang Zhao†,
Alabama A&M University, Huntsville, Alabama, 35762

Sijun Zhang‡
ESI CFD, Inc., Huntsville, Alabama, 35806

and
Yen-Sen Chen§
Applied Research Laboratory, Hsinchu 30078, Taiwan

Lateral nozzle forces are known to cause severe structural damage to any new rocket engine in development during test. While three-dimensional, transient, turbulent, chemically reacting computational fluid dynamics methodology has been demonstrated to capture major side load physics with rigid nozzles, hot-fire tests often show nozzle structure deformation during major side load events, leading to structural damages if structural strengthening measures were not taken. The modeling picture is incomplete without the capability to address the two-way responses between the structure and fluid. The objective of this study is to develop a tightly coupled aeroelastic modeling algorithm by implementing the necessary structural dynamics component into an anchored computational fluid dynamics methodology. The computational fluid dynamics component is based on an unstructured-grid, pressure-based computational fluid dynamics formulation, while the computational structural dynamics component is developed under the framework of modal analysis. Transient aeroelastic nozzle startup analyses at sea level were performed, and the computed transient nozzle fluid-structure interaction physics presented.

---

* Aerospace Engineer, ER42, Fluid Dynamics Branch, Propulsion Structure, Thermal, and Fluids Analysis Division, Senior Member AIAA.
† Associate Professor, Member AIAA.
‡ Technical Fellow, Associate Fellow AIAA.
§ Senior Research Fellow, Associate Fellow AIAA.

Nomenclature

C_1,C_2,C_3,C_μ= turbulence modeling constants, 1.15, 1.9, 0.25, and 0.09.

C = damping

C_p = heat capacity

D = diffusivity

F_{yz}, F_y, F_z = integrated force, and component forces in the lateral direction

f = frequency

H = total enthalpy

K = thermal conductivity or stiffness

k = turbulent kinetic energy

M = mass

Q = heat flux

r = Eigen function

T = temperature

t = time, s

u = mean velocities

V^2 = $\sum u^2$

x = Cartesian coordinates or nondimensional distance

Y = physical displacement

Z = generalized displacement

α = species mass fraction

ε = turbulent kinetic energy dissipation rate

μ = viscosity

μ_t = turbulent eddy viscosity ($=\rho C_\mu k^2/\varepsilon$)

ξ = damping parameter

Π = turbulent kinetic energy production

ρ = density

σ = turbulence modeling constants, 0.9, 0.9, 0.89, and 1.15 for Eqs. (2), (4-6).

τ = shear stress

Φ = mode shape matrix

ω = chemical species production rate or natural frequency

Subscripts

r = radiation

g = mesh movement

t = turbulent flow

I. Introduction

Nozzle lateral forces during engine startup and shutdown transients, if not properly managed, are known to cause severe structural damage to the engine hardware for almost all liquid rocket engines during their initial development [1-4]. Transient nozzle side load is therefore considered a high risk item and a critical design issue. For that reason, many research efforts [5-26] have been devoted to understanding the side load physics and their impact on the magnitude of side loads. For regeneratively-cooled engines such as the Space Shuttle Main Engine (SSME), the peak side load generating physics have been identified as the λ shock oscillations across the nozzle lip [7]. For film-cooled engines such as the Japanese LE-7A engine and the U.S. J-2X engine under development, the major side load generating physics have been associated with the jump of the separation line [3, 8]. Other side load physics such as the Free-Shock Separation (FSS)-to-Restricted-Shock Separation (RSS) transition have been mentioned as the critical physics for the European Vulcain engine [10].

In the aforementioned research efforts, computational fluid dynamics (CFD) have been demonstrated as a powerful analysis and design tool in computing and understanding the underlying transient side load physics. And most of the CFD efforts, have been focused on computing the side load physics with rigid nozzles and not flexible, or aeroelastic nozzles. However, during actual hot-firing of a rocket engine, the nozzle wall or the structure of the nozzle, often flexes or deforms in response to the lateral aerodynamic forces. The deformation of the nozzle wall simultaneously modifies the aerodynamic flowfield and the lateral forces, which in turn affects the nozzle wall deformation. This aeroelastic movement of the nozzle wall, which was not considered in the rigid nozzle modeling, is indeed one of the important side load physics and needs to be considered.

In early 1990's, Pekkari [21] proposed a simplified model to study the aeroelastic stability of the first bending mode of the Vulcain engine. The model consists of an equation of motion describing the displacement of the nozzle wall. For calculation of the aerodynamic load on the wall, a simplified pressure distribution, based on a linearized supersonic flow theory, was used before the separation point. After the separation point, ambient pressure was used. The separation point was established by assuming ratios of separation pressure to ambient pressure as parametric studies. The aerodynamic load calculation of the model was later improved by Östlund [10], where the pressure force applied to the nozzle wall, before the separation point, was extracted from three-dimensional Euler simulations, while the separation point was estimated through an empirical criterion. These two pioneering researches introduced the concept of aeroelastic modeling into nozzle side load studies. In addition, Östlund [10] showed schematically the two asymmetric modes and six buckling modes, which were first visualized in nozzle tests of Tuovila and Land [22].

To follow up on the aeroelastic analysis of Pekkari and Östlund, it appears that two improvements are in order. That is, to refine the simplified wall pressure distribution or the Euler solution on the fluid side by the more accurate full CFD solutions, and to go from addressing the first bending mode on the structure side with more detailed computational structural dynamics (CSD) formulations that could cover more major deformation modes. These improvements were not realized until 2008, when Zhang, et al [25] embarked on probably the first coupled CFD/CSD methodology for aeroelastic nozzle study, by coupling among a full Navier-Stokes solver CFD-FASTRAN, a CSD code FEM-STRESS, and an interface code MDICE, on a quasi-steady, two-dimensional nozzle. In 2013, the same methodology was further demonstrated to show aeroelastic deformation of nozzle wall by Zhao et al. [20], on a quasi-steady, three-dimensional analysis of a J-2S nozzle for 0.1818 s of elapsed time. A short while earlier in 2012, Blades, et al. [26] developed a similar methodology to that of Zhao, et al. [20] and Zhang, et al. [25], by coupling a full Navier-Stokes solver CHEM, a CSD code Abaquas, and an interface code CSE, to demonstrate the aeroelastic deformation of a SSME Block II nozzle transient startup for 0.021 s, started at 0.79 s into the startup transient. These developments represent advances over earlier simple aeroelastic nozzle analyses, however, it is noted that these analyses ignored chemically reacting flows which plays an important role in all transient nozzle physics for engine hot-firing at sea level. In addition, none of these analyses computed at times or chamber pressures at or close to the occurrence of any major side load events. For example, transient times in the analysis of Blades, et

al. ranged from 0.79 s to 0.811 s, which is far from the occurrence of the first major transient nozzle physics for SSME startup transient – the FSS-to-RSS transition.

Engineers at Marshall Space Flight Center and its contractors have been developing a pressure-based, turbulent, chemically reacting flow CFD methodology for computing the rigid-body transient nozzle flows. For example, a transient SSME nozzle flow separation computation invoking system modeling for inlet flow history was first reported in 1992 [24]. The analyses that captured and anchored major side load physics and its peak magnitudes for regenerative cooled SSME nozzle [7] and film cooled J-2X nozzle [8] were reported in 2009. That anchored CFD methodology has been used to support the design and analysis of the current J-2X engine development and selected efforts were published in literatures [8, 9, 19, 23]. With the recent advances in aeroelastic modeling of nozzle side loads [20, 25, 26], and the recognition of the importance of fluid-structure interaction on transient nozzle physics, there is a need to improve our design and analysis methodology by considering the aeroelastic modeling. While examining the recent aeroelastic analyses [20, 25, 26], it occurred to us that the CFD and CSD computations were carried out in different codes and those codes were only connected through an interface code, thus the analyses can only be categorized as loosely coupled aeroelastic solutions [20]. In 2013, Wang, et al. [38] implemented the necessary CSD formulations directly into the anchored CFD code, and demonstrated the tightly coupled fluid-structure interaction algorithms on the transient startup of the SSME Block I engine at sea level, from 2.8 s to 2.876 s – inside the region of λ shock oscillations across the nozzle lip. In this effort, the computations are carried out from the command start to the time of full flow in the nozzle, in order to capture all the major physics during the transient nozzle startup.

II. Computational Methodology

A. Computational Fluid Dynamics

The computational fluid dynamics (CFD) methodology is based on a multi-dimensional, finite-volume, viscous, chemically reacting, unstructured grid, and pressure-based formulation. Time-varying transport equations of continuity, species continuity , momentum, total enthalpy, turbulent kinetic energy, and turbulent kinetic energy dissipation were solved using a time-marching sub-iteration scheme and are written as:

$$\frac{\partial \rho}{\partial t} + \frac{\partial}{\partial x_j}\left[\rho\left(u_j - u_{jg}\right)\right] = 0 \tag{1}$$

$$\frac{\partial \rho \alpha_i}{\partial t} + \frac{\partial}{\partial x_j}\left[\rho\left(u_j - u_{jg}\right)\alpha_i\right] = \frac{\partial}{\partial x_j}\left[\left(\rho D + \frac{\mu_t}{\sigma_\alpha}\right)\frac{\partial \alpha_i}{\partial x_j}\right] + \omega_i \tag{2}$$

$$\frac{\partial \rho u_i}{\partial t} + \frac{\partial}{\partial x_j}\left[\rho\left(u_j - u_{jg}\right)u_i\right] = -\frac{\partial p}{\partial x_i} + \frac{\partial \tau_{ij}}{\partial x_j} \tag{3}$$

$$\frac{\partial \rho H}{\partial t} + \frac{\partial}{\partial x_j}\left[\rho\left(u_j - u_{jg}\right)H\right] = \frac{\partial p}{\partial t} + Q_r + \frac{\partial}{\partial x_j}\left(\left(\frac{K}{C_p} + \frac{\mu_t}{\sigma_H}\right)\nabla H\right) + \frac{\partial}{\partial x_j}\left(\left(\left(\mu + \mu_t\right) - \left(\frac{K}{C_p} + \frac{\mu_t}{\sigma_H}\right)\right)\nabla\left(V^2/2\right)\right) \tag{4}$$

$$+ \frac{\partial}{\partial x_j}\left(\left(\frac{K}{C_p} + \frac{\mu_t}{\sigma_H}\right)\left(u_k\frac{\partial u_j}{\partial x_k} - \frac{2}{3}u_j\frac{\partial u_k}{\partial x_k}\right)\right)$$

$$\frac{\partial \rho k}{\partial t} + \frac{\partial}{\partial x_j}\left[\rho\left(u_j - u_{jg}\right)k\right] = \frac{\partial}{\partial x_j}\left[\left(\mu + \frac{\mu_t}{\sigma_k}\right)\frac{\partial k}{\partial x_j}\right] + \rho\left(\Pi - \varepsilon\right) \tag{5}$$

$$\frac{\partial \rho \varepsilon}{\partial t} + \frac{\partial}{\partial x_j}\left[\rho\left(u_j - u_{jg}\right)\varepsilon\right] = \frac{\partial}{\partial x_j}\left[\left(\mu + \frac{\mu_t}{\sigma_\varepsilon}\right)\frac{\partial \varepsilon}{\partial x_j}\right] + \rho\frac{\varepsilon}{k}\left(C_1\Pi - C_2\varepsilon + C_3\Pi^2/\varepsilon\right) \tag{6}$$

A predictor and corrector solution algorithm was employed to provide coupling of the governing equations. A second-order central-difference scheme was employed to discretize the diffusion fluxes and source terms. For the convective terms, a second-order upwind total variation diminishing difference scheme was used. To enhance the temporal accuracy, a second-order backward difference scheme was employed to discretize the temporal terms. Point-implicit method was used to solve the chemical species source terms. Sub-iterations within a time step were used for driving the system of second-order time-accurate equations to convergence. Details of the numerical algorithm can be found in Ref's [27-30].

An extended k-ε turbulence model [31] was used to describe the turbulence. A modified wall function approach was employed to provide wall boundary layer solutions that are less sensitive to the near-wall grid spacing. Consequently, the model has combined the advantages of both the integrated-to-the-wall approach and the conventional law-of-the-wall approach by incorporating a complete velocity profile and a universal temperature profile [32]. A seven-species, nine-reaction detailed mechanism [32] was used to describe the finite-rate, hydrogen/oxygen afterburning combustion kinetics. The seven species are H_2, O_2, H_2O, O, H, OH, and N_2. The thermodynamic properties of the individual species are functions of temperature. The multiphysics pertinent to this study have been anchored in earlier efforts, (e.g., SSME axial force and wall heat transfer [27], SSME startup side load and dominant shock breathing frequency [7], J-2X startup and shutdown side loads for a nozzlette configuration

[8], nozzle film cooling applications [33], and conjugate heat transfer [34], and separated supersonic flows [7, 8, 19, 23, 24]).

The Arbitrary Lagrangian-Eulerian formulation given above in Eqs (1) - (6) is implemented in the flow solver in a manner that fully satisfies the Discrete Geometric Conservation Laws [35] for each cell in the grid; namely, discrete geometric "closure" of the cell at the start and end of each time step, and exact equality between the sum of the discrete volumes swept by all moving faces of the cell and the discrete change in the volume of the cell. Satisfaction of the second Discrete Geometric Conservation Law ensures that spurious sources and fluxes are not generated by the deformation or motion of cells or cell faces, especially for those adjacent to the moving boundaries. This in turn avoids loss of accuracy in the fluid dynamic computations and in the coupling across the interface between the fluid dynamic and the structural dynamic portions of the problem [20].

B. Computational Structural Dynamics

The structural dynamics response due to fluid flow actions has been analyzed using direct finite-element analysis. The aeroelastic equations of motion of solid bodies are given by

$$[M]\{\ddot{Y}\}+[C]\{\dot{Y}\}+[K]\{Y\}=\{F\} \tag{7}$$

where $\{Y\}$ is the displacement vector, $[M]$ is the mass matrix, $[C]$ is the damping matrix, $[K]$ is the stiffness matrix, and $\{F\}$ is the force vector due to the aerodynamic loads and shear stresses.

The motion Equation (7) of the structure can be solved using modal approach. On the basis of modal decomposition of the structure motion with the eigenvectors of the vibration problem, the displacement, velocity and acceleration can be transformed [25, 35] to the generalized displacement, velocity and acceleration using a transformation matrix, which can be expressed as the following:

$$\{Y\}=[\Phi]\{Z\};\ \{\dot{Y}\}=[\Phi]\{\dot{Z}\};\ \{\ddot{Y}\}=[\Phi]\{\ddot{Z}\} \tag{8}$$

Here [Φ] is the mode shape matrix containing the eigenvectors, orthonormalized with the mass matrix. $\{Z\}, \{\dot{Z}\}, \text{and } \{\ddot{Z}\}$ are the generalized displacement, velocity and acceleration vectors, respectively. The eigenvectors are orthogonal to both mass and stiffness matrixes and if Rayleigh damping is assumed, it is also orthogonal to the damping matrix. Pre-multiplying Equation (8) by $[\Phi]^T$, we get

$$\{\ddot{Z}\}+[\Phi]^T[C][\Phi]\{\dot{Z}\}+[\Phi]^T[K][\Phi]\{Z\}=[\Phi]^T\{F\} \tag{9}$$

where

$$[\Phi]^T[M][\Phi]=1$$

Equation (9) can be written as *n* individual equations, one for each mode, as follows

$$\left.\begin{aligned}&\ddot{z}_i+2\xi_i\omega_i\dot{z}_i+\omega_i^2 z_i=r_i\\&r=\Phi_i^T\{F\}\end{aligned}\right\}\ \mathrm{i}=1,2,...,\mathrm{n} \tag{10}$$

Here ω_i is the natural frequency for the ith mode ξ_i is the corresponding damping parameter for that mode. The solution to Equation (10) can be obtained for each mode using direct integration algorithm. In this effort, since the first several mode shapes are usually important, we chose to compute the first four mode shapes: ovalization, bending, triangle, and square, as shown in Fig. 1. In our current formulation, a structural dynamics software was employed to extract the Eigen modes and Eigen frequencies.

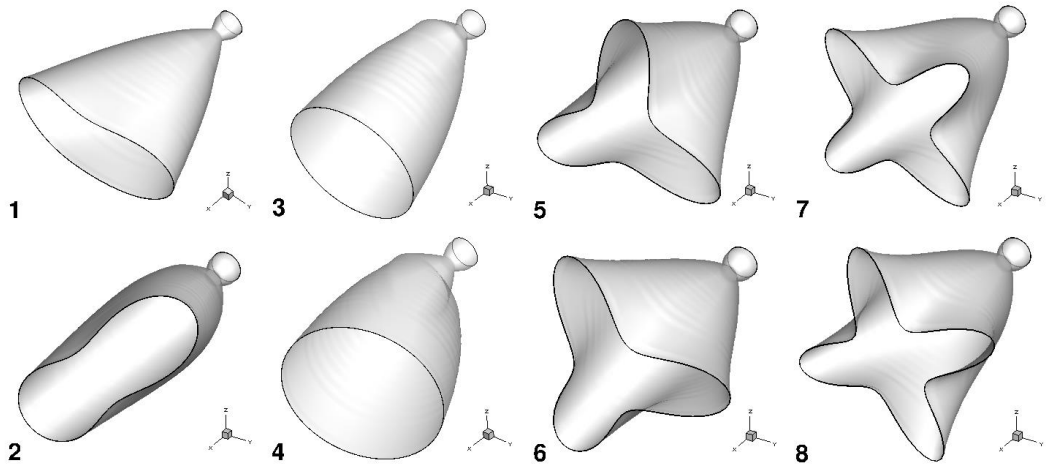

Fig. 1. The four mode shapes.

C. Computational Mesh Dynamics

The geometric and inertial effects of the motions of deforming structures are fed into the flowfield through the varying fluid-dynamic boundary conditions at the surface of structures, which account for the locations and the velocities of these surfaces. In addition, in order to maintain boundary and grid conformity at the fluid-structure interface, the flowfield grid must be deformed to reflect the motion of the fluid-structure interfaces. The new coordinates of the fluid mesh nodes are computed by a computational mesh dynamics procedure. In the present work, the flowfield grid is deformed at every fluid-structure data exchange, which is carried out once at the end of every global time-step, continuously accommodating the deformed shape of the structures in the aeroelastic model. The deformation of the fluid-dynamic grid in this work is accomplished by using a spring analog approach, which is applicable for any type of meshes.

The assumption with the spring analog approach is that the mesh nodes are connected like a network of springs. By performing a force balance on each of the "spring elements", an equilibrium balance is sought which provides a smooth mesh. If two elements (nodes) are too close, the spring force will repel the nodes away from each other. Since each nodal position depends on its neighboring nodes, the boundary deformation effects are felt throughout the mesh domain. Therefore, when the geometries of the

boundary nodes are changed, the distributed spring system settles the interior nodes into a new equilibrium state which can be modeled by

$$\sum_{j=1}^{N_i} k_{ij}(\delta_i - \delta_j) = 0 \tag{11}$$

for all nodes i in the field. In Eq. (11), δi and δj are the coordinate displacements of node i and its neighboring node j, respectively. N_i is the number of neighboring nodes connected to node i, k_{ij} is the spring stiffness for a given edge between i to j which is taken to be inversely proportionally to the length of the edge as

$$k_{ij} = \frac{1.}{\sqrt{(x_i - x_j)^2 + (y_i - y_j)^2 + (z_i - z_j)^2}} \tag{12}$$

D. Transient Startup Sequences

Transient system-level simulation is a vital part of the computational methodology, because it provides the time-histories of the inflow properties entering the nozzle. Simply put, the ramp rates, or histories, of the inlet pressure, fluid temperature and species concentrations play an important role in determining the type of flow physics, magnitude and duration of the flow physics during the transient operations. In other words, the time-varying inlet flow properties determine the residence times of the flow physics inside the nozzle.

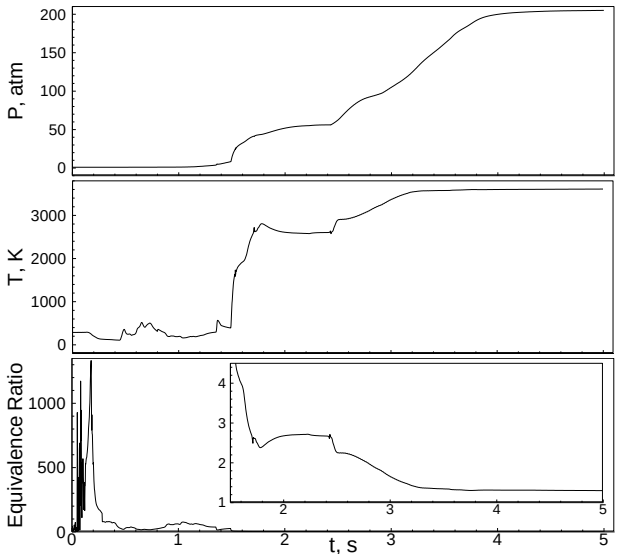

Fig. 2 Computed thruster chamber inlet properties during the start-up transient.

The system-level simulation is based on a

lumped, control-volume approach to model the rocket engine as a network of components and sub-components. This method of transient system-level modeling has been shown to be effective in simulating the low-frequency, transient physics associated with the operation of previous and existing rocket engines [SSME, rocket liquid (RL-10), integrated power demonstrator, etc.] and therefore, is an important tool in the design and planning of sequencing the transient events of rocket engine operation. Figure 2 shows the major inlet flow properties obtained from the system model: the time-varying inlet pressure, temperature, and equivalence ratio profiles. These time-varying inlet properties were used at the injector faceplate of the thrust chamber for the CFD computation. Two significant pressure rise events can be identified in the inlet pressure history of Fig. 2. The first one occurs at 1.5 s due to oxygen prime, while the second one occurs at about 2.4 s, caused by the step opening of the oxygen valves in the pre-burners. The inlet temperature history shows a sharp jump at 1.5 s, leveling off after 1.75 s, jumps a little bit again at 2.4s, and increases linearly until around 3.1 s when it reaches the final temperature. The inlet equivalence ratio history shows that the thruster environment is fuel rich throughout the start-up transient, especially in the first 1.5 s, setting up the potential for afterburning. That turns out to be the source of the combustion wave, because the pressure jump at 1.5 s increases the reaction rate of afterburning, which leads to the generation of the combustion wave. Afterburning plays an important part in the subsequent asymmetric flow physics such as the shock transitions and shock breathings across the nozzle lip. As mentioned in the beginning of this section, that the route or history between the starting and end points of any of the curves in Fig. 2 influences the flow physics intimately, any simplification on any part of the sequence may run the risk of missing or degradation of important flow physics. This SSME start transient process involves thermal-fluid physics phenomena and safety-based operating practices that are typical of a conventional liquid hydrogen/liquid oxygen rocket engine.

III. Computational Grid Generation

This section will be completed when the final manuscript is due.

IV. Boundary and Inlet Conditions

Since SSME is a first stage engine, fixed freestream boundary conditions were set corresponding to sea level. No-slip condition was specified for the solid walls. Time-varying inlet flow boundary conditions were used at the main

combustion chamber (MCC) inlet. These inlet flow properties obtained from the engine system simulation include the time varying total pressure, temperature and propellant compositions. The time varying propellant composition was preprocessed with the Chemical Equilibrium Calculation program [36], assuming the propellants were ignited to reach equilibrium composition immediately beyond the injector faceplate. The larger than unity equivalence ratio throughout the 5 s ramp period indicates the SSME is operated at fuel rich condition and the inlet composition contains mostly steam and excess hydrogen, as shown in Fig. 2. At the start command, or time zero, the entire flowfield was initialized with quiescent air. The presence of air allows the afterburning with the excess fuel which contributes to the side force physics.

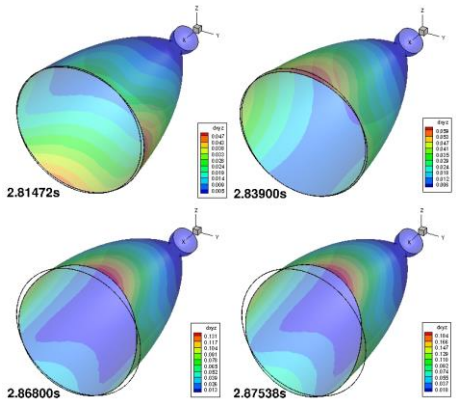

Figure 3 Side views of computed nozzle shape and deformation contours.

V. Results and Discussion

This section will be completed when the final manuscript is due. Figure 3 shows side views of computed nozzle shape and deformation contours at four time slices.

VI. Conclusion

This section will be completed when the final manuscript is due.

Acknowledgments

The first author was partially supported by the J-2X engine program at NASA Marshall Space Flight Center, in which Mike Shadoan managed the nozzle project and Marcus Neely managed the system test project. Professor Zhao was partially supported by a Seed Grant from National Science Foundation and by a NASA 2012 Summer Faculty Fellowship. The authors acknowledge James Beck of Pratt-Whitney Rocketdyne for his insight in fluid-structure interactions. The authors also wish to thank Eric Blades of ATA Engineering for several initial discussions.

References

[1] Nave, L.H., and Coffey, G.A., "Sea Level Side Loads in High-Area-Ratio Rocket Engines," AIAA Paper 73-1284, Nov. 1973.

[2] Cikanek, H.A., "Characteristics of Space Shuttle Main Engine Failures," AIAA Paper 87-1939, June 1987.

[3] Watanabe, Y., Sakazume, N., and Tsuboi, M., "LE-7A Engine Nozzle Problems During the Transient Operations," AIAA Paper 2002-3841, July 2002.

[4] Shi, J., "Rocket Engine Nozzle Side Load Transient Analysis methodology – A Practical Approach," AIAA Paper 2005 – 1860, April 2005.

[5] Hagemann, G., Terhardt, M., Frey, M., Reijasse, P., Onofri, M., Nasuti, F., and Ostlund, J., "Flow Separation and Side-Loads in Rocket Nozzles," 4th International Symposium on Liquid Space Propulsion, March 12-15, 2000, DLR Lampoldshausen, pp. 1-19.

[6] Yonezawa, K., Yokota, K., Tsujimoto, K., Sakazume, N., and Watanabe, Y., "Three-Dimensional Unsteady Flow Simulation of Compressed Truncated Perfect nozzles," AIAA Paper 2002-3991, July 2002.

[7] Wang, T.-S., "Transient Three-Dimensional Startup Side Load Analysis of a Regeneratively Cooled Nozzle," *Shock Waves – An International Journal on Shock Waves, Detonations and Explosions.* Vol. 19, Issue 3, 2009, pp. 251~264. DOI: 10.1007/s00193-009-0201-2.

[8] Wang, T.-S., and Guidos, M., "Transient Three-Dimensional Side Load Analysis of a Film-Cooled Nozzle," *Journal of Propulsion and Power,* Vol. 25, No. 6, 2009, pp. 1272-1280, doi: 10.2514/1.41025.

[9] Wang, T.-S., Lin, J., Ruf, J., Guidos, M., and Cheng, G.C., "Effect of Coolant Flow Distribution on Transient Side Load of Film Cooled Nozzles," *Journal of Propulsion and Power,* Vol. 28, No. 5, September-October, 2012, pp. 1081-1090. doi:10.2514/1.B34397

[10] Östland, J., "Supersonic Flow Separation with Application to Rocket Engine Nozzles," Doctoral Thesis, Royal Institute of Technology, Stockholm, Department of Mechanics, Sweden, 2004.

[11] Deck, S., "Delayed Detached Eddy Simulation of the End-Effect Regime and Side-Loads in an Overexpanded Nozzle Flow," *Shock Waves – An International Journal on Shock Waves, Detonations and Explosions.* Vol. 19, Issue 3, 2009, pp. 239~249. DOI: 10.1007/s00193-009-0199-5.

[12] Hadjada, A., and Onofri, M., "Nozzle Flow Separation," *Shock Waves – An International Journal on Shock Waves, Detonations and Explosions.* Vol. 19, Issue 3, 2009, pp. 163~169. DOI: 10.1007/s00193-009-0209-7.

[13] Tomita, T., Takahashi, M., Sasaki, M., Sakamoto, H., Takahashi, M., Tamura, H., "Experimental Evaluation of Side Loads in LE-7A Prototype Engine Nozzle," *Shock Waves – An International Journal on Shock Waves, Detonations and Explosions.* Vol. 19, Issue 3, 2009, pp. 213~228. DOI: 10.1007/s00193-009-0191-0.

[14] Nguyen, A.T., Deniau, H., Girard, S., and De Roquefort, T.A., "Unsteadiness of Flow Separation and End-Effects Regime in a Thrust-Optimized Contour Rocket Nozzle," Flow, Turbulence and Combustion, Vol. 71, No. 1-4, 2003, pp.161-181.

[15] Deck S., and Guillen, P., "Numerical Simulation of Side loads in an Ideal Truncated Nozzle," *Journal of Propulsion and Power*, Vol. 18, No. 2, 2002, pp. 261-269. doi: 10.2514/2.5965

[16] Shimizu, T., Miyajima, H., and Kodera, M., "Numerical Study of Restricted Shock Separation on a Compressed Truncated Perfect Nozzle," *AIAA Journal*, Vol. 44, No. 3, 2006, pp. 576-584.

[17] Stark, R., and Genin, C., "Optimisation of a Rocker Nozzle Side Load Reduction Device," AIAA Paper 2012-3970, July 2012.

[18] Reijasse, Ph., and Boccaletto, L., "Influence of Film Cooling on Nozzle Side loads," AIAA Paper 2008-392, Jan. 2008.

[19] Wang, T.-S., Lin, J., Ruf, J., and Guidos, M., "Transient Three-Dimensional Side Load Analysis of Out-of-Round Film Cooled Nozzles," *Journal of Propulsion and Power*, Vol. 27, No. 4, July-August, 2011, pp. 899-907, doi: 10.2514/1.B34082.

[20] Zhao, X., Bayyuk, S., and Zhang, S.J., "Aeroelastic Response of Rocket Nozzles to Asymmetric Thrust Loading", Computer and Fluids, Vol. 76, 2013, pp. 128-148.

[21] Pekkari, L.-O., "Aeroelastic Analysis of Side Load in Supersonic Nozzles with Separated Flow." AIAA Paper 1994-3377, June 1994.

[22] Tuovila, W.J., and Land, N.S., "Experimental Study of Aeroelastic Instability of Overexpanded Rocket Nozzle Extensions," NASA TN D-4471, 1968.

[23] Wang, T.-S., Lin, J., and Guidos, M., "Transient Side-Load Analysis of Out-of-Round Film-Cooled Nozzle Extensions," *Journal of Propulsion and Power*, (2013), accessed June 5, 2013. doi: http://arc.aiaa.org/doi/abs/10.2514/1.B34812

[24] Wang, T.-S., "Numerical Study of the Transient Nozzle Flow Separation of Liquid Rocket Engines," *Computational Fluid Dynamics Journal*, Vol.1, No.3, Oct. 1992, pp. 319-328.

[25] Zhang, S.J., Fuchiwaki, T., and Zhao, X., "Aeroelastic Coupling and Side Load in Rocket Nozzles," AIAA Paper 2008-4064, 2008.

[26] Blades, E.L., Luke, E.A., and Ruf, J., "Fully Coupled Fluid-Structure Interaction Simulations of Rocket Engine Side Loads," AIAA Paper 2012-3969, July 2012.

[27] Wang, T.-S., "Multidimensional Unstructured-Grid Liquid Rocket Engine Nozzle Performance and Heat Transfer Analysis," *Journal of Propulsion and Power*, Vol. 22, No. 1, January-February, 2006, pp. 78-84.

[28] Shang, H.M., and Chen, Y.-S., "Unstructured Adaptive Grid method for Reacting Flow Computation," AIAA Paper 1997-3183, July 1997.

[29] Wang, T.-S., Chen, Y.-S., Liu, J., Myrabo, L.N., and Mead, F.B. Jr., "Advanced Performance Modeling of Experimental Laser Lightcraft," *Journal of Propulsion and Power*, Vol. 18, No. 6, 2002, pp. 1129-1138.

[30] Chang, G., Ito, Y., Ross, D., Chen. Y.-S., Zhang S., and Wang, T.-S., "Numerical Simulations of Single Flow Element in a Nuclear Thermal Thrust Chamber" AIAA Paper 2007-4143, June 2007.

[31] Chen, Y.-S., and Kim, S. W., "Computation of Turbulent Flows Using an Extended k-ε Turbulence Closure Model," NASA CR-179204, Oct. 1987.

[32] Wang, T.-S., Droege, A., D'Agostino, M., Lee, Y.-C., and Williams, R., "Asymmetric Base-Bleed Effect on X-33 Aerospike Plume Induced Base-Heating Environment," *Journal of Propulsion and Power*, Vol. 20, No. 3, 2004, pp. 385-393.

[33] Chen, Y.-S., Cheng, G.C., and Farmer, R.C., "Reacting and Non-Reacting Flow Simulation for Film Cooling in 2-D Supersonic Flows," AIAA Paper 92-3602, July 1992.

[34] Wang, T.-S., Canabal, F., Chen, Y.-S., and Cheng, G.C., "Multiphysics Computational Analysis of a Solid-Core Nuclear Thermal Engine Thrust Chamber," *Journal of Propulsion and Power*, Vol. 26, No. 3, May-June, 2010, pp. 407-414.

[35] Thomas, P. and Lombard, C., "Geometric Conservation Law and its Application to Flow Computations on Moving Grids," *AIAA Journal, AIAA*, Vol. 17, No. 10, 1979, pp. 1030-1037.

[36] Svehla, R.A., McBride, B.J., "FORTRAN IV Computer Program for Calculation of Thermodynamic and Transport Properties of Complex Chemical Systems," NASA TN D-7056, (1973)

[37] Giosan, Ioan. "Dynamic Analysis with Damping for Free Standing Structures using Mechanical Event Simulation." University Politehnica of Bucharest Scientific Bulletin, Series C: Electrical Engineering 68.3 (2006): pp. 15-30.

[38] Wang, T.-S., Zhao, X., Zhang, S.J., "Development of an Aeroelastic Modeling Capability for Transient Nozzle Side Load Analysis," AIAA Paper 2013-3641, July 2013.